



Numerical modeling of the formation of Shackleton crater at the lunar south pole

Samuel H. Halim^{a,*}, Natasha Barrett^b, Sarah J. Boazman^{c,d}, Aleksandra J. Gawronska^e, Cosette M. Gilmour^f, Harish^{g,h}, Katie McCanaanⁱ, Animireddi V. Satyakumar^j, Jahnavi Shah^{k,l}, David A. Kring^{m,n}

^a Department of Earth and Planetary Sciences, Birkbeck, University of London, London, UK

^b Department of Earth and Atmospheric Sciences, University of Alberta, Edmonton, Alberta, Canada

^c Department of Earth Sciences, Natural History Museum, London, UK

^d Department of Earth Sciences, University College London, London, UK

^e Department of Geology and Environmental Earth Science, Miami University, Oxford, Ohio, USA

^f Centre for Research in Earth and Space Science, York University, Toronto, Ontario, Canada

^g Planetary Sciences Division, Physical Research Laboratory, Ahmedabad, India

^h Discipline of Earth Sciences, Indian Institute of Technology, Gandhinagar, India

ⁱ Department of Earth and Environmental Sciences, University of Manchester, Manchester, UK

^j CSIR – National Geophysical Research Institute (CSIR-NGRI), Hyderabad, India

^k Department of Earth Sciences, University of Western Ontario, London, Ontario, Canada

^l The Institute for Earth and Space Exploration, University of Western Ontario, London, Ontario, Canada

^m Lunar and Planetary Institute, Universities Space Research Association, Houston, Texas, USA

ⁿ NASA Solar System Exploration Research Virtual Institute, USA

ABSTRACT

The lunar south pole, on the rim of Shackleton crater, is the target for the next human landing on the Moon. We use numerical modeling to investigate the formation of that crater and the distribution of ejecta around the south pole. We find that a 1.5 km diameter asteroid with a chondrite-like composition, vertically impacting a gabbroic anorthositic target at 15 km/s, forms a crater morphologically similar to Shackleton. If the impact had a shallower 45-degree trajectory, the asteroid may have had a diameter of 1.75 km and velocity of 15 km/s or a diameter of 1.5 km and velocity of 20 km/s. Impact melt is generated during the impact, with most of the melt volume ponding on the crater floor. We introduce a water-bearing layer at various depths in the target and find that the burial depth of a volatile layer influences the final crater morphology and may explain the morphology of Shackleton.

1. Introduction

Shackleton crater is a key area of interest for future lunar exploration due to its proximity to the South Pole-Aitken (SPA) basin and near coincidence with the south pole (Fig. 1a). Shackleton is a simple crater with a mean rim diameter of 21 km and depth of 4.2 km (Haruyama et al., 2008; Spudis et al., 2008; Zuber et al., 2012; Tye et al., 2015) and has a greater depth to diameter (d/D) ratio (0.195 ± 0.025 , Zuber et al., 2012) than other simple craters in the south polar region (Rubanenko et al., 2019). This bowl-shaped, near-axisymmetric crater has unusually well-preserved crater walls and rim crest (Haruyama et al., 2008; Zuber et al., 2012). The projectile that formed Shackleton impacted into a

platform-like massif, resulting in a crater with a regional topographic tilt (Spudis et al., 2008). Originally, Shackleton was estimated to be approximately 1.1 to 3.3 billion years old (Wilhelms, 1987); however, this age was determined using the apparent freshness of the crater, which can be misleading due to low solar incidence angles. Subsequent crater counting analysis suggests an Imbrian age of $\sim 3.6 \pm 0.4$ Ga (Spudis et al., 2008). More recent observations using data from the Lunar Orbiter Laser Altimeter (LOLA) (Smith et al., 2010) yielded an age of ~ 3.69 Ga for the ejecta and ~ 1.44 Ga for the steep crater walls (Zuber et al., 2012). The crater floor is a permanently shadowed region (PSR) creating a potential cold-trap for volatiles to accumulate over time (Watson et al., 1961; Arnold, 1979; Campbell and Campbell, 2006;

* Corresponding author.

E-mail addresses: shalim03@mail.bbk.ac.uk (S.H. Halim), nbarrett@ualberta.ca (N. Barrett), s.boazman@nhm.ac.uk (S.J. Boazman), gawronaj@miamioh.edu (A.J. Gawronska), cgilmour@yorku.ca (C.M. Gilmour), harishnandal77@gmail.com (Harish), kathryn.mccanaan@manchester.ac.uk (K. McCanaan), satyageo41@gmail.com (A.V. Satyakumar), jshah68@uwo.ca (J. Shah), Kring@lpi.usra.edu (D.A. Kring).

<https://doi.org/10.1016/j.icarus.2020.113992>

Received 26 October 2019; Received in revised form 25 June 2020; Accepted 21 July 2020

Available online 29 July 2020

0019-1035/© 2020 The Authors.

Published by Elsevier Inc.

This is an open access article under the CC BY-NC-ND license

(<http://creativecommons.org/licenses/by-nc-nd/4.0/>).

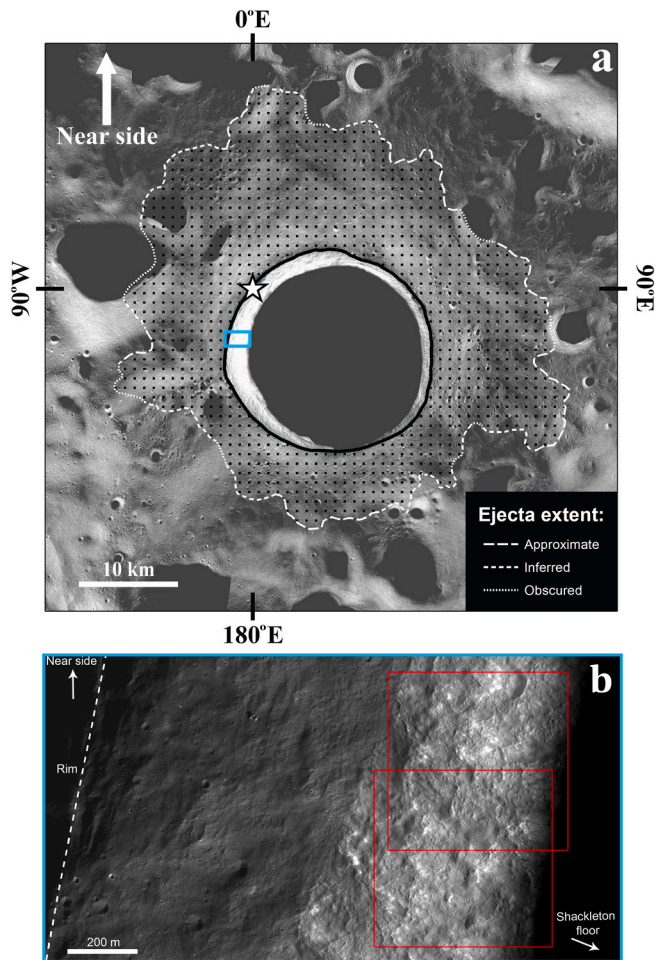


Fig. 1. Geographical and geological context of Shackleton (21 km diameter). (a) White lines show potential extent of the ejecta blanket mapped using 388 Lunar Reconnaissance Orbiter Camera (LROC) Narrow Angle Camera (NAC) images. Lines are overlying the NAC averaged mosaic (1 m/pixel). White star indicates the south pole. (b) Detail of NAC images M133786042L and M146833333L. Blue box represents the highlighted area from (a) showing high albedo purest anorthosite (PAN) units (red boxes) in the crater wall, initially identified by Yamamoto et al. (2012).

Haruyama et al., 2008; Spudis et al., 2008; Zuber et al., 2012). The estimated age for the current orientation of the Moon's spin axis and present pole location indicate that the floor has been in permanent shadow for ~ 2 Ga (Ward, 1975; Siegler et al., 2016) and, thus, Shackleton could have been accumulating volatiles over this time. The likely source for these volatiles is implantation from solar wind (Crider and Vondrak, 2000, 2002; Starukhina, 2001) and, potentially, late-stage volcanism (Kring et al., 2014; Needham and Kring, 2017).

Due to the presence of potential volatiles in PSRs, the south polar region and Shackleton crater are primary targets for future human exploration efforts on the Moon. These resources may be essential for developing a sustainable and long-term human presence on the lunar surface (e.g., Spudis and Lavoie, 2010) including further investigation of the SPA basin. The SPA basin is the oldest and largest impact basin on the lunar surface. The impact event which created Shackleton may have excavated part of a massif previously formed by the SPA basin impact, providing a unique probe of massif formation and potentially exposures of primitive lunar crust. Thus, missions to the lunar south pole may help address several scientific priorities (Concepts 1, 2, 3, 4, and 6; NRC, 2007).

We simulate impacts into the lunar surface to determine the likely conditions that produced Shackleton. These simulations allow us to

investigate crater morphology, ejecta distribution, and impact melt generation from such an impact. As volatiles may have been deposited in the polar regions, we also investigate the consequences that a volatile layer in the target may have for final crater geomorphology. Any volatiles in the pre-impact target at the lunar south pole were likely to exist in the form of a regolith-ice mixture (Nozette et al., 2001; Thomson et al., 2012), preserved in PSRs, and buried under ejecta layers sourced from surrounding, older craters such as Haworth, Shoemaker, and Faustini. Indeed, layers of debris are observed in the walls of Shackleton crater on one side of the crater (Gawronska et al., 2020; Harish et al., 2020). Therefore, we investigate the influence that a mixed regolith-volatile layer has on the final crater morphology when placed at varying depths within the target. We then compare the simulated crater geomorphologies to the current morphology of Shackleton to determine whether volatiles on or beneath the surface were present at the time of impact.

2. Methods

The impact-Simplified Arbitrary Lagrangian Eulerian (iSALE) shock physics code (Collins et al., 2004; Wünnemann et al., 2006), based on the SALE hydrocode (Amsden et al., 1980), was used to compute impact simulations. iSALE has been well tested against laboratory experiments (Wünnemann et al., 2006) and other impact modeling codes (Pierazzo et al., 2008). It has been used extensively to model lunar impacts over a variety of scales (e.g., Potter et al., 2012a, 2012b, 2013a, 2013b, 2015, 2018; Miljković et al., 2013, 2016; Kring et al., 2016; Silber et al., 2017; Wiggins et al., 2019). Simulations were constructed in an axisymmetric half-space, taking advantage of two-dimensional (2D) cylindrical geometry to save computational time. The 2D version of iSALE limits impact trajectories to 90° (vertical). A 3D code could be used to evaluate a more probable impact angle (most likely 45°) but would either be too computationally expensive or reduce spatial resolution. Previous work has shown that 2D models produce the reasonable azimuthally average behavior of impacted materials for circa 45° (e.g., Pierazzo and Melosh, 2000; Elbeshhausen et al., 2009; Davison et al., 2011).

The simulations explored impact velocities between 10 and 20 km/s to capture an appropriate range of those for the Moon (Ivanov, 2008). Simple scaling approximations suggested an impactor diameter of ~ 1.5 km, so simulations explored diameters between 1 and 2 km. Each simulation was run for 500 s beyond initial impact to fully capture the crater-forming process. Computational cell size was fixed at 50 m with the cells per projectile radius (cpr) being varied between 10 and 20 in order to model the projectile radius. Increasing the cpr would be more computationally expensive and crater morphology has been shown to be minimally affected compared to resolutions greater than 20 cpr (Silber et al., 2017 and references therein). We conducted a resolution test to confirm this finding, varying the resolution of the models between 10 and 100 cpr. Due to the computational time needed to process these simulations, transient crater measurements were compared at a simulated time of 25 s. The results (Table 1) show the near convergence of each parameter at 100 cpr. The values for transient crater radius, depth, and volume using a resolution of 15 cpr are underestimated by 1.4%, 4.1%, and 6.9%, respectively, compared to 100 cpr simulations. Therefore, we can say that while the dimensions related to crater

Table 1

Resolution test with transient crater dimensions taken at time, $t = 25$ s.

Resolution (cpr)	Radius (km)	Depth (km)	Volume (km ³)
10	6.31	5.54	448.78
15	6.46	5.55	468.11
20	6.47	5.56	477.96
50	6.53	5.77	491.79
75	6.54	5.81	499.05
100	6.55	5.83	502.93

morphology are systemically underestimated at lower resolution, the overall crater morphology is still accurately represented at the resolution used in this study. The model grid was composed of a high-resolution zone with dimensions of 350 horizontal cells (17.5 km) by 300 vertical cells (15 km). Cells beyond the high-resolution zone increased in size by a factor of 1.05 per cell to maximum distances of 38.5 km horizontally, 30 km below the point of impact, and 7 km above the target. Simulated crater morphologies were compared to the observed morphology of Shackleton, especially 2D profiles generated by LOLA topography data. Criteria used to determine best-fit crater morphologies included: rim-to-rim diameter, floor diameter, rim-to-floor depth, rim height above the pre-impact surface, rim crest shape, slope of walls, and topography of the plains outside of the rim crest.

Shackleton's depth (4.2 km) justified use of a 30 km deep crustal target with no mantle layer beneath. Crustal thickness at the south pole (28 to 32 km, [Wieczorek et al., 2013](#)) illustrates that the lunar mantle is at a depth that would not significantly affect the crater formation process in these simulations. A Tillotson equation of state (EoS) for gabbroic anorthosite ([Ahrens and O'Keefe, 1977](#)) was used to represent the crustal target, and a semi-analytical equation of state (ANEOS) of dunite ([Benz et al., 1989](#)) for the impactor. Anorthosite was chosen based on purest anorthosite (PAN) units inferred by [Yamamoto et al. \(2012\)](#) using Kaguya Spectral Profiler ([Ohtake et al., 2008](#)) data, some of which were identified in the crater wall during this study ([Fig. 1b](#)). We used a constant thermal profile with a gradient of 10 K/km, similar to those used in previous lunar impact studies ([Miljković et al., 2013](#); [Zhu et al., 2015](#); [Potter et al., 2018](#)). Most impactors are chondritic and dunite has been proven as a relatively accurate proxy for chondritic asteroidal material ([Pierazzo et al., 1997](#)).

Once a crater with Shackleton's morphology was produced in an anorthositic crust, a water-rich layer was added to the target to investigate the effect of volatile layers on crater morphology. An idealized, 100 m thick water-ice saturated regolith layer was added to the anorthosite target (similar, in part, to the method used by [Senft and Stewart, 2007](#)) at varying depths: on the surface, buried at 100 m, and buried at 500 m. A Tillotson EoS for wet tuff, based on a Nevada tuff with a water content of 14.4 wt% ([Allen, 1967](#)), was used to simulate a volatile-saturated sediment layer (density = 1970 kg/m³). Although this water content is greater than the 5.6 ± 2.9 wt% water content estimated in the regolith at the Lunar CRater Observing and Sensing Satellite (LCROSS) impact site ([Colaprete et al., 2010](#)), it serves to investigate the effects of a water-rich layer in the regolith. Wet tuff has been used previously in terrestrial impact simulations that required modeling of a water-saturated sediment layer overlying a competent bedrock ([Collins and Wünnemann, 2005](#); [Wünnemann et al., 2005](#); [Kenkmann et al., 2009](#)). The strength and damage models used here are described in [Collins et al. \(2004\)](#) and [Ivanov et al. \(2010\)](#), respectively. Details of the parameters used in this study are listed in Table S1.

A bulk density of 2400 kg/m³ was chosen to represent the crustal material, informed by the Gravity Recovery and Interior Laboratory (GRAIL) mission ([Zuber et al., 2013](#)). Bulk crustal densities are estimated to be ~2600 kg/m³ at the south pole ([Wieczorek et al., 2013](#)) and ~2200 kg/m³ averaged across the highlands ([Besserer et al., 2014](#)); therefore, we used an average to estimate the density of the pre-impact surface at Shackleton. The desired bulk density was obtained using an epsilon-alpha porous compaction model within iSALE ([Wünnemann et al., 2006](#); [Collins et al., 2011](#)), incorporating a porosity of 18.4%, higher than the crustal average for the Moon (~12%). However, this is within the range of regional variations for highland surface porosity ([Wieczorek et al., 2013](#); [Besserer et al., 2014](#)) and feldspathic samples returned from the Apollo missions ([Kiefer et al., 2012](#)). Similarly, a bulk density of 2400 kg/m³ was chosen for the dunite impactor based on the average bulk density of chondritic meteorites ([Britt and Consolmagno, 2003](#); [Wilkison et al., 2003](#); [Consolmagno et al., 2008](#)) and similarly-sized parent body asteroids (e.g., Itokawa and 1999 KW4 α/β) to those modeled in this work (~0.5 to 2 km diameter) ([Abe et al., 2006](#); [Ostro](#)

[et al., 2006](#)). Porosity of the impactor was modeled at 27.5%, well within the expected range of macro-porosities for chondrite parent body asteroids ([Flynn et al., 1999](#); [Abe et al., 2006](#)).

Lagrangian tracer particles placed in each cell of the high-resolution zone tracked the path followed by the material within that cell throughout the simulation. For each simulation, pressure and temperature were recorded at the location of each tracer. In the best-fit crater simulation, a simple impact melt volume was calculated by using tracer pressures and temperatures at the end of the simulation. Instantaneous liquidus temperatures were calculated using the Simon approximation ([Poirier, 1991](#)) and volumes of cells with tracers that experienced temperatures greater than the calculated melt temperature were added to the melt volume. This assumes only material above the liquidus is molten and, therefore, underestimates the total melt produced compared to melt volumes if partially molten material was considered. Latent heat of melting is not considered in the EoS used, which means melt volumes may be anomalously large. Additionally, peak pressures will be underestimated for the resolution of these simulations and temperatures in regions experiencing shock pressures between 15 and 100 G-pascals (GPa) are underestimated in the low-pressure phase of the anorthosite Tillotson EoS ([Ahrens and O'Keefe, 1977](#)). To estimate whether melt volumes produced by the simulations are reliable and realistic, we compare the results with melt volumes calculated using scaling laws ([Abramov et al., 2012](#)) for the same scenario. Impact melts were not considered for layered targets. Vapor production during impact was not important, so material with a density <300 kg/m³ was removed to expedite computation time.

The block oscillation acoustic fluidization model ([Melosh, 1979](#); [Melosh and Ivanov, 1999](#)) was used in the simulations, implemented using parameters based on scaling relations described by [Wünnemann and Ivanov \(2003\)](#) and the approach used by [Silber et al. \(2017\)](#). A constant gravitational acceleration field of 1.62 m/s² was used in all simulations.

3. Results

3.1. Final crater morphology

A total of 20 scenarios were simulated, 17 with a solid target and 3 with a layered target. For impacts into a homogenous target, first, a 1 km diameter projectile impacting at 10 km/s produced a crater that was too small in both depth and diameter. Increasing the diameter of the low-velocity projectile initially led to a better fitting crater diameter (~20 km), but too shallow (~3 km). Further increasing this projectile diameter (up to 2 km) led to crater diameters well over 25 km. Secondly, a high-velocity projectile (20 km/s) with a 2 km diameter resulted in a crater that was too wide and deep. Using a smaller projectile diameter (1 km) formed a crater with a depth comparable to Shackleton but a diameter of ~18 km. Increasing the projectile diameter formed final crater depths and floor diameters that were too large, even if the rim diameter was comparable to Shackleton. Finally, impactor velocity was set to 15 km/s and diameters varied between 1 and 1.5 km, culminating in the simulation of a best-fit crater with morphology most similar to the observed morphology of Shackleton.

[Fig. 2](#) illustrates the crater-forming process for the best-fit simulation of Shackleton. An impactor with a diameter of 1.5 km and a velocity of 15 km/s, which resulted in an impact energy of 4.89×10^{20} J, was determined to form a crater similar in morphology to that of Shackleton. After 500 s, the final crater was deemed to have formed completely. A maximum transient crater depth of 5.26 km was reached 25 s into the simulation ([Fig. 2b](#)), at which point the excavation stage of the crater forming process ceased. After this, the target surface began to rebound, initializing the formation of the breccia lens and final crater floor. However, the volume of the transient crater increased until 61 s, with a maximum of 447 km³. Rim uplift and distribution of the ejecta curtain over the target surface are seen to continue through [Fig. 2b](#) and [c](#). Uplift

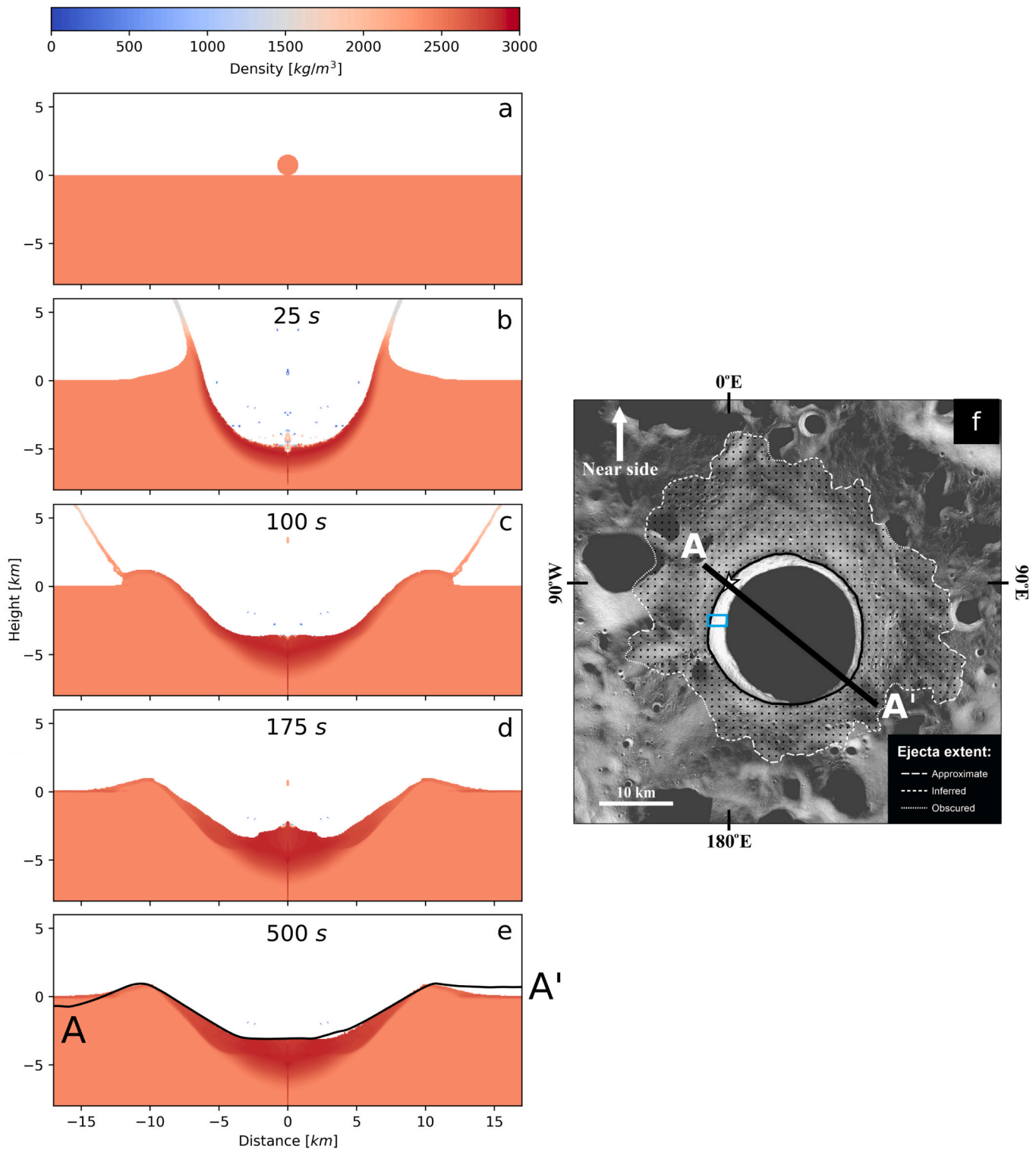


Fig. 2. Density plot for the best-fit simulation for Shackleton crater, progressing from (a) the initiation of impact through to (e) 500 s post-impact. Black line in plot (e) shows a topographical profile of Shackleton crater measured along the line A-A' shown in (f) using a LOLA Digital Elevation Model (DEM) (5 m/pixel).

of the crater floor continued until after the proximal ejecta blanket had been deposited (Fig. 2d) forming what looked like a central peak; however, by the end of the simulation the uplifted material relaxed and formed a flat crater floor (Fig. 2e). The final crater depth, floor diameter, and rim to rim diameter were 4.1, 7.2, and 20.7 km, respectively, which results in a d/D ratio of 0.20. These values agree well with observations

of Shackleton (Zuber et al., 2012), as illustrated in Fig. 2e. The breccia lens extends to a maximum depth of ~ 2.9 km beneath the impact point, reducing in thickness away from the center of the crater as shown by the high-density area (dark material) in Fig. 2e. The systematic underestimation of the transient depth and diameter of craters modeled at this lower resolution, alongside evidence for little modification (<300 m

change in depth) of Imbrian aged craters with diameters >10 km and wall slopes of $\sim 30^\circ$ from degradation simulations (Craddock and Howard, 2000), justifies matching the post-impact simulations to the present day observations of Shackleton. The topographical differences in the target surface beyond the rim can be attributed to the irregularity of the real pre-impact surface, the presence of volatile layers (discussed later), and the limitations of 2D simulations.

Expanding the high-resolution zone of the simulation to 35 km from the impact site (originally 17.5 km) allowed assessment of the ejecta blanket. Ejecta thickness was calculated by measuring the number of cells which contained material at the end of the simulation (500 s post-impact) and multiplying by the cell size (50 m). This process was repeated and recorded at multiple distances from the crater rim where changes in ejecta thickness were observed. Continuous ejecta was deposited ~ 20 km from the crater rim, with discontinuous ejecta travelling farther (up to the boundary of the simulation grid). This agrees well with scaling laws estimating continuous ejecta distribution to one crater diameter beyond the rim, although the outer portions of that ejecta are not readily identifiable in visual images (Fig. 1a). It is likely that, due to the age of Shackleton (~ 3.6 Ga), impact gardening of the regolith has obscured those portions of the ejecta blanket. Ejecta thicknesses at distances 5, 13, and 20 km from the rim are 150, 100, and 50 m thick, respectively. The coarse cell size (50 m) prohibits a more accurate quantification of ejecta thickness.

3.2. Impact melt generation

For the best-fit simulation crater, an impact melt volume of ~ 20 km³ was calculated at 500 s (Fig. 3a). This can be considered the minimum

melt produced during the simulation as it only considered material that still recorded temperatures greater than the instantaneous melt temperature at 500 s. Therefore, any material that may have been heated beyond this melt temperature but had subsequently cooled would not be included in the melt volume calculation. The melt was concentrated in the floor of the target, centered beneath the impact site. Fig. 3b illustrates the maximum extent of the melt distribution across Shackleton based upon tracers that experienced peak temperatures that exceeded 1513 K (solidus of the target material) at any time during the simulation. The maximum melt volume calculated from these tracers was ~ 62 km³, concentrated in the crater floor; however, melt material is also deposited on the crater wall and rim (Fig. 3b). For the calculation of the maximum melt volume, melt material concentrated beneath the crater floor (~ 26 km³) constitutes 42% of the total melt volume generated by the impact. Therefore, while most of the melt material is distributed onto the crater walls, rim, and beyond, the largest single concentration of melt material is likely found in the crater floor.

For a crater of this size, melting occurs from the surface to a depth of ~ 1.6 km in the target rocks. Because the target area is a highland region, not too dissimilar to that of the Apollo 16 landing site, melt compositions will nominally be feldspathic – reflecting the observed PAN seen in Shackleton's crater walls (Yamamoto et al., 2012; Gawronska et al., 2020; Gilmour et al., 2020; Harish et al., 2020). We note, however, that more mafic components ejected from the SPA basin are possible (Kring, 2019; Moriarty and Petro, 2020) and that geologic units beneath the anorthosite are not visible in the crater walls because they are permanently shadowed. Thus, some uncertainty is attached to any current estimate of melt composition.

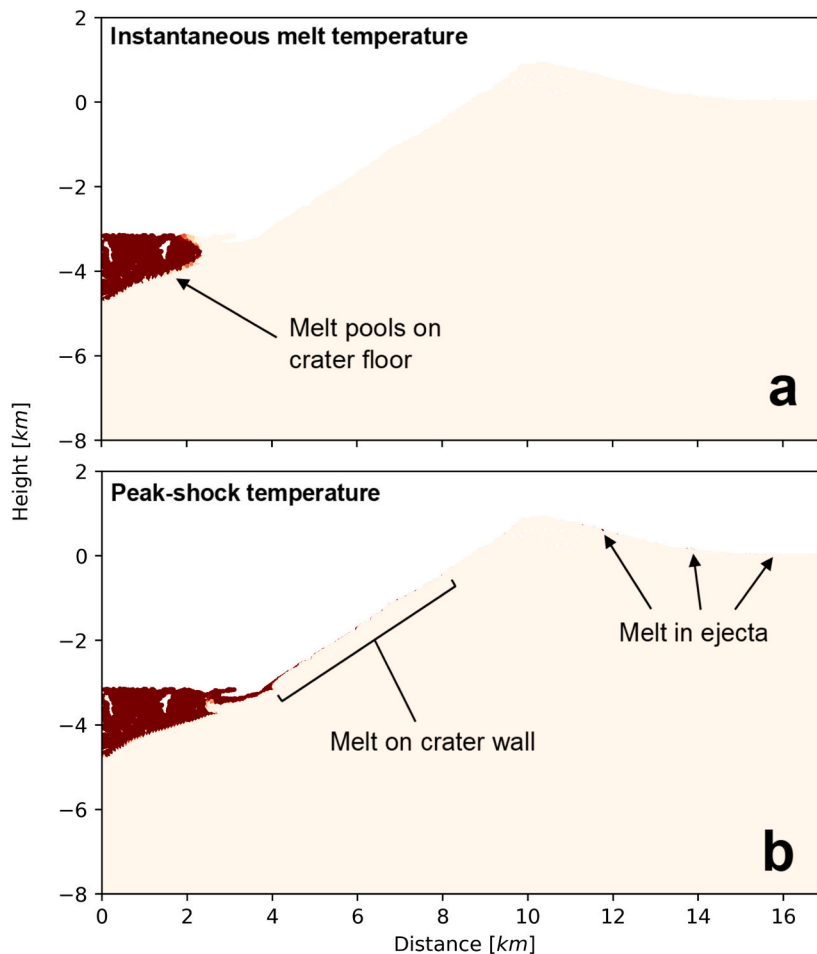


Fig. 3. The minimum and maximum extent of impact melt generated for the best-fit simulation of Shackleton's formation. (a) Red material represents tracers at 500 s with temperatures greater than instantaneous melt temperature of the material. (b) Red material represents tracers which have experienced peak temperatures greater than the material solidus (1513 K) at any point during the simulation. All shades of red represent melt. Lighter shades of red represent material close to, but beneath the boundary of the solidus or instantaneous melt temperature.

3.3. Volatile target layers

Once a best-fit simulation for Shackleton was determined using a homogenous target layer, a mixed volatile-sediment layer with a thickness of 100 m (at a temperature of 125 K) was added at various depths to explore the consequences ice-bearing regolith may have on the morphology of the crater. Fig. 4 illustrates a comparison between the best-fit simulation with no layer (left of each sub-figure) against simulations with the additional volatile layer (right of each sub-figure). A volatile layer at the surface (Fig. 4b), buried at 100 m (Fig. 4c), and buried at 500 m (Fig. 4d) led to final craters with d/D ratios of 0.20, 0.20, and 0.18 respectively. Increasing the burial depth of the volatile layer initially leads to a more pronounced and steeper outer rim (Fig. 4b, c). This is probably due to the rapid removal and potential vaporization of the less dense, weaker volatile layer. Energy from the projectile is consumed by this process and leads to non-ballistic motion of the ejecta blanket, with a greater volume of ejecta deposited non-uniformly closer to the rim. However, at a burial depth of 500 m (Fig. 4d) the rim height decreases, becomes less distinct, and the surface topography flattens when compared to a homogenous target. The inclusion of a volatile layer at any depth does not significantly affect the crater floor depth, relative to the pre-impact surface (height = 0 km, Fig. 4). However, due to the significant decrease in peak rim height, the maximum depth of the final crater (measured from the peak height of the rim to the crater floor) in Fig. 4d is significantly decreased by ~500 m (3.6 km depth) relative to the simulation with a homogenous target layer (4.1 km depth). In all the simulations, volatile layers located beneath the impact site were removed or vaporized. The 500 m buried volatile layer in Fig. 4d shows greater preservation closer to the rim than the 100 m buried layer and surface layer.

4. Discussion

Impact melt volumes derived from post-processing of simulation results agree well with those calculated using scaling laws (Abramov et al., 2012). For purposes of this comparison, we utilize (Abramov et al., 2012; Eq. 12):

$$V_{melt} = 0.12 E_m^{-0.85} \left(\frac{\rho_p}{\rho_t} \right)^{-0.28} D_{tc}^{3.85} g^{0.85} \sin^{1.3} \theta \quad (1)$$

where V_{melt} is the volume of melt produced, E_m is the specific internal energy of the target material at a shock pressure that results in melting upon release, ρ_p and ρ_t are the density of the projectile and target, respectively, D_{tc} is the diameter of the transient crater, g is the acceleration due to gravity, and θ is the angle of impact (where θ is defined as 90° for a vertical impact). We used a value for E_m of 3.42×10^6 J/kg for an anorthosite target material (Bjorkman and Holsapple, 1987) and all other parameter values were taken directly from the iSALE simulations. Using those input values and a 90° angle of impact produces a melt volume of 20.9 km^3 , which corresponds well with the minimum impact melt volume of $\sim 20 \text{ km}^3$ for a vertical impact in the iSALE simulation, estimated by extracting temperature data from tracers placed in the simulation. If we use the scaling relationship to explore melt production with the most likely impact angle of 45° —while keeping the transient and final crater diameters the same—we derive a minimum melt volume of $\sim 13 \text{ km}^3$.

Shackleton's asymmetric crater-rim morphology across the profile A-A' (Fig. 5) shows a more pronounced rim crest in the south pole area (white star on Fig. 5) and a less pronounced, flatter crest and flank on the opposite side. The latter may be consistent with a PSR and/or volatile deposits in the target area. The flatter, less pronounced rim crest and target surface beyond are observed in the scenario with a 100 m thick volatile layer buried at a depth of 500 m (Fig. 4d). This simulation with a buried layer of ice-filled regolith reduces rim height and, thus, is

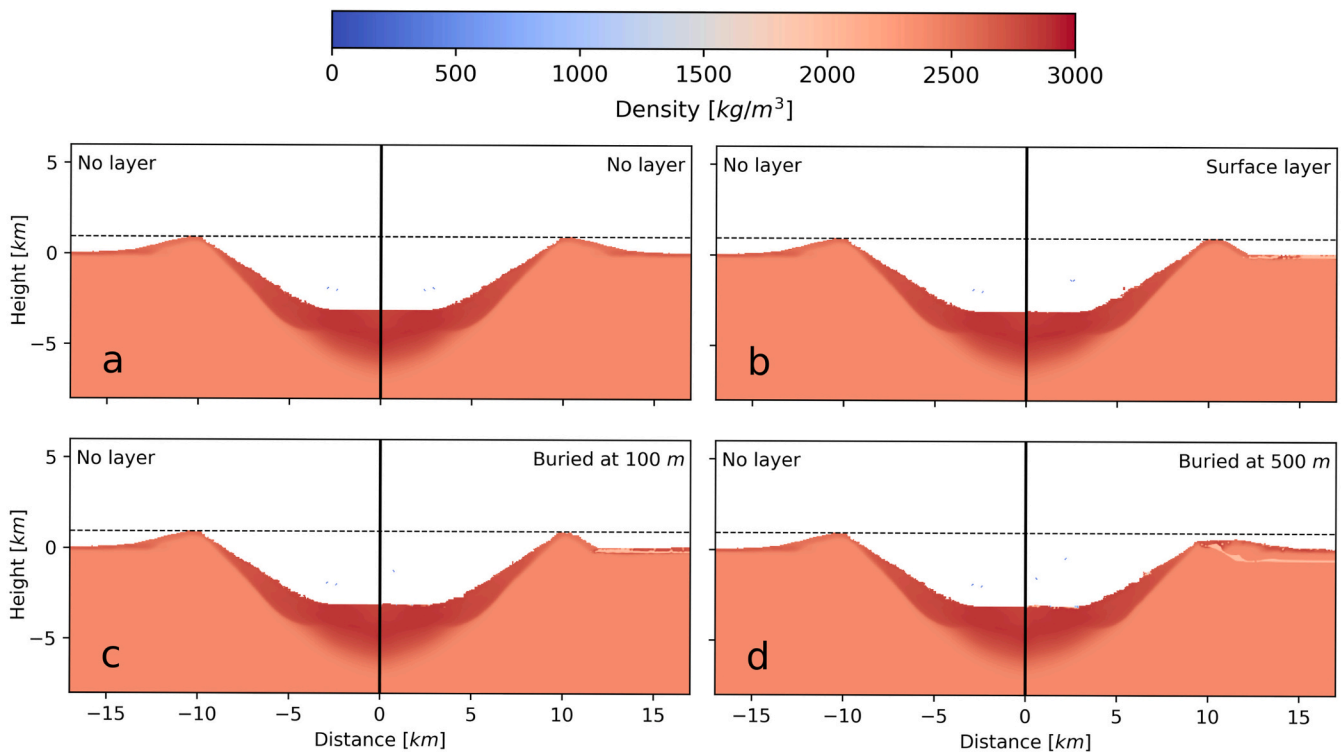


Fig. 4. Comparative density plots for the final crater morphology of the best fit for Shackleton crater (left) against the same simulation with the introduction of a 100 m thick volatile layer (right) for each plot (a-d). Layer placement: (a) no layer, (b) on the surface, (c) buried at 100 m and (d) buried at 500 m. Dashed line shows the maximum height of the rim crest for the homogenous scenario (left). The volatile layer buried at 500 m in (d) is more clearly seen in Fig. 5.

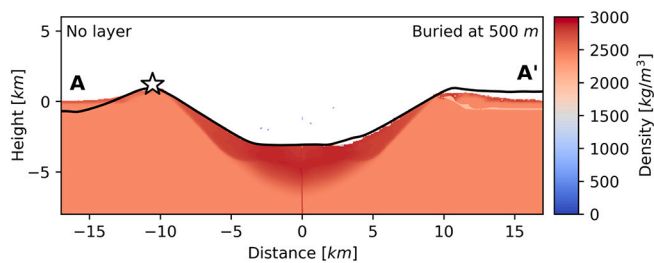


Fig. 5. Density plot to represent the asymmetric surface structure at the impact site. The final crater morphology for a target surface with a homogenous target layer (left) and a target layer with a 100 m thick volatile layer buried at 500 m (right) are displayed. Overlaid is the LOLA topographical profile (black line) shown in Fig. 2. White star = approximate location of the south pole.

consistent with a premise suggested by Kokhanov et al. (2015) that craters in the lunar polar regions are systematically less deep than those in other areas of the Moon. They infer that low temperatures and the presence of a near-surface volatile layer may be responsible for these morphometric differences, although the scale of craters examined differs by more than an order of magnitude compared to Shackleton (0.1 to 1 km diameters compared to 21 km, respectively). As the iSALE simulations explore crater formation, not post-impact modification, they cannot address another model proposed by Rubanenko et al. (2019), in which post-impact infilling of a regolith-ice mixture reduces the depth of the crater. However, we note that if the Rubanenko model is correct, and because Shackleton has a d/D of 0.20, marginally lower than the Stopar et al. (2017) value of 0.21 (for a large dataset of lunar craters up to 10 km), that implies there would be an ice layer no more than ~ 300 m in thickness at the bottom of Shackleton crater.

The geomorphological features of Shackleton may be explained by a combination of subsurface volatiles and pre-impact surface topography. The simulated crater profile (Fig. 5) is offset by ~ 200 m from the topographical surface of Shackleton (black line) on the A' side of the crater. This could be explained by the regional tilt of the pre-impact surface, with the regional slope of the massif on which Shackleton lies estimated to be on the order of 15° or less (Spudis et al., 2008). The rim crest at the south pole agrees best with a target surface with no volatile layer; however, based on the LOLA topographic data and assessment of the NAC imagery used to produce the ejecta map in Fig. 1a, the pre-impact surface topography beyond the rim crest has influenced the slope away from the crater. We infer from the simulations that a combination of pre-impact surface topography (resulting in the regional tilt across Shackleton) and subsurface volatile layers (resulting in the flattened rim crest and flank) could be responsible for the variable crater morphology seen today. The slight disagreement with the profile in the right side of the crater floor in Fig. 5 is potentially explained by slumping of crater wall material onto the floor, which can be seen in LOLA topography (Zuber et al., 2012) and Kaguya imagery (Haruyama et al., 2008, 2013), and may also have been influenced by a weak volatile-sediment mixture in that side of the target.

It is important to note, however, that subsurface volatile layers and pre-impact surface topography are not the only factors that can affect the geomorphology of an impact crater. Indeed, a variety of properties relating to the target material can influence the crater forming process; e.g., heterogeneity in the target rocks (O'Keefe et al., 2001; Senft and Stewart, 2007); changes in material composition (Pierazzo et al., 2008; Miljković et al., 2013); strength (Bray et al., 2008; Potter et al., 2015); and porosity (Wünnemann et al., 2006; Milbury et al., 2015). A distinct type of layered unit has been recently observed in a portion of Shackleton crater's walls (Gawronska et al., 2020; Harish et al., 2020), which may modify composition and porosity, while also providing the conditions needed for deposition of water ice at depth. Thus, water ice at depth is not a unique solution for Shackleton's asymmetrical morphology, but it is shown here, for the first time, to be a parameter

than can alter crater morphologies in the polar regions of the Moon.

5. Conclusions

Our simulations show that Shackleton crater is likely formed by a ~ 1.5 km diameter chondrite-like impactor, impacting with a vertical velocity of ~ 15 km/s. A minimum impact melt volume of ~ 20 km³ is likely to have been produced at a 90° impact angle (decreasing to ~ 13 km³ at 45° using scaling laws) with distribution concentrated solely in the crater floor, directly beneath the point of impact. For the maximum melt volume calculated (~ 62 km³), a significant volume of melt (58% of the total volume) was distributed on the crater walls and outside of the rim crest. The actual distribution of melt material is likely to be somewhere between these scenarios. The asymmetric rim crest heights and topography across the crater may have been influenced by the presence of subsurface volatile layers, pre-impact surface topography, or a combination of both. Specifically, a 100 m thick volatile layer buried at 500 m in the pre-impact surface on one side of the target area (i.e., the side opposite the south pole) is consistent with a relatively flat rim in that area compared with that around the south pole. Higher resolution simulations and better constraints on volatiles present at Shackleton will help to improve the accuracy and robustness of the simulations presented here.

Acknowledgements

We gratefully thank Boris Ivanov, Jay Melosh, Gareth Collins, Kai Wünnemann, and Dirk Elbeshausen for their work in the development of iSALE. Some diagrams in this manuscript were made using the post-processing tool pySALEPlot, developed by Tom Davison. We also thank Satoru Yamamoto for the coordinates of the spectrally identified PAN in the crater wall.

This work was carried out through the 2019 Exploration Science Summer Intern Program hosted by the Lunar and Planetary Institute (LPI) and Johnson Space Center (JSC). This work was supported by NASA Solar System Exploration Research Virtual Institute contracts NNA14AB07A and 80NSSC20M0016 (PI David A. Kring). LPI Contribution No. 2442.

The iSALE shock physics code is not fully open-source: it is distributed on a case-by-case basis to academic users in the impact community, for noncommercial use only. A description of the application requirements can be found at the iSALE website (http://www.isale-code.de/redmine/projects/isale/wiki/Terms_of_use). Data relating to the input parameters of the simulations can be found in the supporting information, specifically Table S1.

We thank two anonymous reviewers and Prof. H. J. Melosh for their helpful comments and suggestions, and Prof. O. Aharonson for editorial handling.

Declaration of Competing Interest

None.

Appendix A. Supplementary data

Supplementary data to this article can be found online at <https://doi.org/10.1016/j.icarus.2020.113992>.

References

- Abe, M., et al., 2006. Mass and local topography measurements of Itokawa by Hayabusa. *Science* 312, 1334. <https://doi.org/10.1126/science.1125718>.
- Abramov, O., Wong, S., Kring, D.A., 2012. Differential melt scaling for oblique impacts on terrestrial planets. *Icarus* 218 (2), 906–916. <https://doi.org/10.1016/j.icarus.2011.12.022>.

- Ahrens, T.J., O'Keefe, J.D., 1977. Equations of state and impact induced shock-wave attenuation on the moon. In: *Impact and Explosion Cratering*. Pergamon, New York, pp. 639–656.
- Allen, R.T., 1967. Equations of state of rocks and minerals. Interim report to NASA under contract DA 49-146-XZ-462. Gen. Dyn. Rep. #GA MD-7834.
- Amsden, A.A., Ruppel, H.M., Hirt, C.W., 1980. SALE: A Simplified ALE Computer Program for Fluid Flow at All Speeds. US Department of Commerce, National Technical Information Service.
- Arnold, J.R., 1979. Ice in the lunar polar regions. *J. Geophys. Res.* 84, 5659–5668.
- Benz, W., Cameron, A.G.W., Melosh, H.J., 1989. The origin of the moon and the single-impact hypothesis III. *Icarus* 81, 113–131. [https://doi.org/10.1016/0019-1035\(89\)90129-2](https://doi.org/10.1016/0019-1035(89)90129-2).
- Besserer, J., Nimmo, F., Wieczorek, M.A., Weber, R.C., Kiefer, W.S., McGovern, P.J., 2014. GRAIL gravity constraints on the vertical and lateral density structure of the lunar crust. *Geophys. Res. Lett.* 41, 5771–5777. <https://doi.org/10.1002/2014GL060240>.
- Bjorkman, M.D., Holsapple, K.A., 1987. Velocity scaling impact melt volume. *Int. J. Impact Eng.* 5, 155–163.
- Bray, V., Collins, G.S., Morgan, J., Schenk, P., 2008. The effect of target properties on crater morphology: comparison of central peak craters on the moon and Ganymede. *Meteorit. Planet. Sci.* 43 (12), 1979–1992. <https://doi.org/10.1111/j.1945-5100.2008.tb00656.x>.
- Britt, D.T., Consolmagno, G.J., 2003. Stony meteorite porosities and densities: a review of the data through 2001. *Meteorit. Planet. Sci.* 38, 1161–1180. <https://doi.org/10.1111/j.1945-5100.2003.tb00305.x>.
- Campbell, B.A., Campbell, D.A., 2006. Regolith properties in the south polar region of the moon from 70-cm radar polarimetry. *Icarus* 180 (1), 1–7. <https://doi.org/10.1016/j.icarus.2005.08.018>.
- Colaprete, A., et al., 2010. Detection of water in the LCROSS ejecta plume. *Science* 330, 463–468. <https://doi.org/10.1126/science.1186986>.
- Collins, G.S., Wünnemann, K., 2005. How big was the Chesapeake Bay impact? Insight from numerical modeling. *Geology* 33 (12), 925–928. <https://doi.org/10.1130/G21854.1>.
- Collins, G.S., Melosh, H.J., Ivanov, B.A., 2004. Modeling damage and deformation in impact simulations. *Meteorit. Planet. Sci.* 39 (2), 217–231. <https://doi.org/10.1111/j.1945-5100.2004.tb00337.x>.
- Collins, G.S., Melosh, H.J., Wünnemann, K., 2011. Improvements to the ϵ - α porous compaction model for simulating impacts into high-porosity solar system objects. *Int. J. Impact Eng.* 38 (6), 434–439. <https://doi.org/10.1016/j.ijimpeng.2010.10.013>.
- Consolmagno, G.J., Britt, D.T., Macke, R.J., 2008. The significance of meteorite density and porosity. *Chemie der Erde—Geochemistry* 68, 1–29. <https://doi.org/10.1016/j.chemer.2008.01.003>.
- Craddock, R., Howard, A., 2000. Simulated degradation of lunar impact craters and a new method for age dating farside mare deposits. *J. Geophys. Res. Planets* 105 (E8), 20387–20401. <https://doi.org/10.1029/1999je001099>.
- Crider, D., Vondrak, R., 2000. The solar wind as a possible source of lunar polar hydrogen deposits. *J. Geophys. Res. Planets* 105, 26773–26782. <https://doi.org/10.1029/2000je001277>.
- Crider, D., Vondrak, R., 2002. Hydrogen migration to the lunar poles by solar wind bombardment of the moon. *Adv. Space Res.* 30, 1869–1874. [https://doi.org/10.1016/s0273-1177\(02\)00493-3](https://doi.org/10.1016/s0273-1177(02)00493-3).
- Davison, T.M., Collins, G.S., Elbeshhausen, D., Wünnemann, K., Kearsley, A., 2011. Numerical modeling of oblique hypervelocity impacts on strong ductile targets. *Meteorit. Planet. Sci.* 46, 1510–1524. <https://doi.org/10.1111/j.1945-5100.2011.01246.x>.
- Elbeshhausen, D., Wünnemann, K., Collins, G.S., 2009. Scaling of oblique impacts in frictional targets: implications for crater size and formation mechanisms. *Icarus* 204, 716–731. <https://doi.org/10.1016/j.icarus.2009.07.018>.
- Flynn, G.J., Moore, L.B., Klöck, W., 1999. Density and Porosity of Stone Meteorites: Implications for the Density, Porosity, Cratering, and Collisional Disruption of Asteroids. *Icarus* 142 (1), 97–105. <https://doi.org/10.1006/icar.1999.6210>.
- Gawronska, A.J., Barrett, N., Boazman, S.J., Gilmour, C.M., Halim, S.H., Harish, McCanaan, K., Satyakumar, A.V., Shah, J., Meyer, H.M., Kring, D.A., 2020. Geologic context and potential EVA targets at the lunar south pole. *Advances in Space Research* 66 (6), 1247–1264. <https://doi.org/10.1016/j.asr.2020.05.035>.
- Gilmour, C.M., et al., 2020. Artemis 2024: potential EVA targets at the lunar south pole. *Lunar Planet. Sci. Li*, abstract #1482.
- Harish, et al., 2020. Two types of terrain exposed in the upper crater wall of Shackleton crater, lunar south pole: implications for future landings. *Lunar Planet. Sci. Li*, Abstract #1148.
- Haruyama, J., Ohtake, M., Matsunaga, T., Morota, T., Honda, C., Yokota, Y., 2008. Lack of exposed ice inside lunar south pole Shackleton crater. *Science* 322 (5903), 938–939. <https://doi.org/10.1126/science.1164020>.
- Haruyama, J., Yamamoto, S., Yokota, Y., Ohtake, M., Matsunaga, T., 2013. An explanation of bright areas inside Shackleton crater at the lunar south pole other than water-ice deposits. *Geophys. Res. Lett.* 40, 3814–3818. <https://doi.org/10.1002/grl.50753>.
- Ivanov, B.A., 2008. Size-frequency distribution of asteroids and impact craters: Estimates of impact rate. In: Adushkin, V.V., Nemchinov, I.V. (Eds.), *Catastrophic Events Caused by Cosmic Objects*. Springer-Verlag, Berlin, pp. 91–116. https://doi.org/10.1007/978-1-4020-6452-4_2.
- Ivanov, B.A., Melosh, H.J., Pierazzo, E., 2010. Basin-forming impacts: reconnaissance modeling. In: Reimold, W.U., Gibson, R.L. (Eds.), *Large Meteorite Impacts and Planetary Evolution IV*, 465. Geological Society of America, pp. 29–49. <https://doi.org/10.1130/2010.2465/03>.
- Kenkmann, T., Collins, G.S., Wittmann, A., Wünnemann, K., Reimold, W.U., Melosh, H.J., 2009. A model for the formation of the Chesapeake Bay impact crater as revealed by drilling and numerical simulation. In: Gohn, G.S., Koeberl, C., Miller, K.G., Reimold, W.U. (Eds.), *The ICDP-USGS Deep Drilling Project in the Chesapeake Bay Impact Structure: Results from the Eyreville Core Holes*: Geological Society of America Special Paper 458, pp. 571–585. [https://doi.org/10.1130/2009.2458\(25\)](https://doi.org/10.1130/2009.2458(25)).
- Kiefer, W.S., Macke, R.J., Britt, D., Irving, A.J., Consolmagno, G., 2012. The density and porosity of lunar rocks. *Geophys. Res. Lett.* 39, L07201 <https://doi.org/10.1029/2012GL051319>.
- Kokhanov, A., Kreslavsky, M., Karachevtseva, I., 2015. Small impact craters in the polar regions of the moon: peculiarities of morphometric characteristics. *Sol. Syst. Res.* 49 (5), 295–302. <https://doi.org/10.1134/s0038094615050068>.
- Kring, D.A., 2019. Lunar south pole geology: Preparing for a seventh landing. In: *NASA Exploration Science Forum, Abstract #NESF2019-127b*.
- Kring, D.A., Kramer, G.Y., Bussey, D.B.J., Hurley, D.M., 2014. Prominent volcanic source of volatiles in the south polar region of the Moon. In: Paper presented at Annual Meeting of the Lunar Exploration Analysis Group (2014). Lunar and Planetary Institute, Laurel, Maryland.
- Kring, D.A., Kramer, G.Y., Collins, G.S., Potter, R.W.K., Chandnani, M., 2016. Peak-ring structure and kinematics from a multi-disciplinary study of the Schrödinger impact basin. *Nat. Commun.* 7, 13161. <https://doi.org/10.1038/ncomms13161>.
- Melosh, H.J., 1979. Acoustic fluidization: a new geologic process. *J. Geophys. Res.* 84, 7513–7520.
- Melosh, H.J., Ivanov, B.A., 1999. Impact crater collapse. *Ann. Rev. Earth Planet. Sciences* 27, 385–415. <https://doi.org/10.1146/annurev.earth.27.1.385>.
- Milbury, C., et al., 2015. Preimpact porosity controls the gravity signature of lunar craters. *Geophys. Res. Lett.* 42 (22), 9711–9716. <https://doi.org/10.1002/2015gl066198>.
- Miljković, K., et al., 2013. Asymmetric distribution of lunar impact basins caused by variations in target properties. *Science* 342 (6159), 724–726. <https://doi.org/10.1126/science.1243224>.
- Miljković, K., et al., 2016. Subsurface morphology and scaling of lunar impact basins. *J. Geophys. Res. Planets* 121 (9), 1695–1712. <https://doi.org/10.1002/2016je005038>.
- Moriarty, D.P., Petro, N.E., 2020. Mineralogical diversity of the lunar south pole: critical context for future sample return goals and interpretation. *Lunar Planet. Sci. Li*, abstract #2428.
- National Research Council, 2007. *The Scientific Context for Exploration of the Moon*. The National Academies Press, Washington, DC. <https://doi.org/10.17226/11954>.
- Needham, D.H., Kring, D.A., 2017. Lunar volcanism produced a transient atmosphere around the ancient moon. *Earth Planet. Sci. Lett.* 478, 175–178. <https://doi.org/10.1016/j.epsl.2017.09.002>.
- Nozette, S., Spudis, P.D., Robinson, M.S., Bussey, D.B.J., Lichtenberg, C., Bonner, R., 2001. Integration of lunar polar remote-sensing data sets: evidence for ice at the lunar south pole. *J. Geophys. Res.* 106 (10), 23253–23266. <https://doi.org/10.1029/2000JE001417>.
- Ohtake, M., Haruyama, J., Matsunaga, T., Yokota, Y., Morota, T., Honda, C., LISM Team, 2008. Performance and scientific objectives of the SELENE (KAGUYA) multiband imager. *Earth Planets Space* 60, 257–264. <https://doi.org/10.1186/BF03352789>.
- O'Keefe, J., Stewart, S., Lainhart, M., Ahrens, T., 2001. Damage and rock-volatile mixture effects on impact crater formation. *Int. J. Impact Eng.* 26 (1–10), 543–553. [https://doi.org/10.1016/s0734-743x\(01\)00112-9](https://doi.org/10.1016/s0734-743x(01)00112-9).
- Ostro, S., et al., 2006. Radar imaging of binary near-earth asteroid (66391) 1999 KW4. *Science* 314 (5803), 1276–1280. <https://doi.org/10.1126/science.1133622>.
- Pierazzo, E., Melosh, H.J., 2000. Melt production in oblique impacts. *Icarus* 145, 252–261. <https://doi.org/10.1006/icar.1999.6332>.
- Pierazzo, E., Vickery, A.M., Melosh, H.J., 1997. A reevaluation of impact melt production. *Icarus* 127 (2), 408–423. <https://doi.org/10.1006/icar.1997.5713>.
- Pierazzo, E., et al., 2008. Validation of numerical codes for impact and explosion cratering: impacts on strengthless and metal targets. *Meteorit. Planet. Sci.* 43 (12), 1917–1938. <https://doi.org/10.1111/j.1945-5100.2008.tb00653.x>.
- Poirier, J., 1991. *Introduction to the Physics of the Earth's Interior*, 264 Pp. Cambridge University Press, Cambridge, U.K.
- Potter, R.W.K., Kring, D.A., Collins, G.S., Kiefer, W.S., McGovern, P.J., 2012a. Estimating transient crater size using the crustal annular bulge: insights from numerical modeling of lunar basin-scale impacts. *Geophys. Res. Lett.* 39, L18203 <https://doi.org/10.1029/2012GL052981>.
- Potter, R.W.K., Collins, G.S., Kiefer, W.S., McGovern, P.J., Kring, D.A., 2012b. Constraining the size of the south pole-Aitken basin impact. *Icarus* 220, 730–743. <https://doi.org/10.1016/j.icarus.2012.05.032>.
- Potter, R.W.K., Kring, D.A., Collins, G.S., Kiefer, W.S., McGovern, P.J., 2013a. Numerical modeling of the formation and structure of the Orientale impact basin. *J. Geophys. Res. Planets* 118, 963–979. <https://doi.org/10.1002/jgre.20080>.
- Potter, R.W.K., Kring, D.A., Collins, G.S., 2013b. Quantifying the attenuation of structural uplift beneath large lunar craters. *Geophys. Res. Lett.* 40 (21), 5615–5620. <https://doi.org/10.1002/2013gl057829>.
- Potter, R.W.K., Kring, D.A., Collins, G.S., 2015. Scaling of basin-sized impacts and the influence of target temperature. In: Osinski, G.R., Kring, D.A. (Eds.), *Large Meteorite Impacts and Planetary Evolution V*, 518. Geological Society of America, pp. 99–113. [https://doi.org/10.1130/2015.2518\(06\).Special.Paper](https://doi.org/10.1130/2015.2518(06).Special.Paper).
- Potter, R.W.K., Head, J.W., Guo, D., Liu, J., Xiao, L., 2018. The Apollo peak-ring impact basin: insights into the structure and evolution of the south pole-Aitken basin. *Icarus* 306, 139–149. <https://doi.org/10.1016/j.icarus.2018.02.007>.
- Rubanenko, L., Venkatraman, J., Paige, D., 2019. Thick ice deposits in shallow simple craters on the moon and mercury. *Nat. Geosci.* 12 (8), 597–601. <https://doi.org/10.1038/s41561-019-0405-8>.

- Senft, L., Stewart, S., 2007. Modeling impact cratering in layered surfaces. *J. Geophys. Res.* 112, E11002 <https://doi.org/10.1029/2007je002894>.
- Siegler, M.A., et al., 2016. Lunar true polar wander inferred from polar hydrogen. *Nature* 531 (7595), 480–484. <https://doi.org/10.1038/nature17166>.
- Silber, E.A., Osinski, G.R., Johnson, B.C., Grieve, R.A.F., 2017. Effect of impact velocity and acoustic fluidization on the simple-to-complex transition of lunar craters. *J. Geophys. Res. Planets* 122, 800–821. <https://doi.org/10.1002/2016JE005236>.
- Spudis, P.D., Lavoie, T., 2010. Mission and implementation of an affordable lunar return. In: *Space Manufacturing 14 Conference*. Space Studies Institute.
- Smith, D.E., Zuber, M.T., Jackson, G.B., et al., 2010. The Lunar Orbiter Laser Altimeter Investigation on the Lunar Reconnaissance Orbiter Mission. *Space Sci. Rev.* 150, 209–241. <https://doi.org/10.1007/s11214-009-9512-y>.
- Spudis, P.D., Bussey, B., Plescia, J., Josset, J., Beauvivre, S., 2008. Geology of Shackleton crater and the south pole of the moon. *Geophys. Res. Lett.* 35 (14) <https://doi.org/10.1029/2008GL034468>.
- Starukhina, L., 2001. Water detection on atmosphereless celestial bodies: alternative explanations of the observations. *J. Geophys. Res. Planets* 106, 14701–14710. <https://doi.org/10.1029/2000je001307>.
- Stopar, J., et al., 2017. Relative depths of simple craters and the nature of the lunar regolith. *Icarus* 298, 34–48. <https://doi.org/10.1016/j.icarus.2017.05.022>.
- Thomson, B.J., et al., 2012. An upper limit for ice in Shackleton crater as revealed by LRO mini-RF orbital radar. *Geophys. Res. Lett.* 39, L14201 <https://doi.org/10.1029/2012GL051119>.
- Tye, A.R., et al., 2015. The age of lunar south circumpolar craters Haworth, shoemaker, Faustini, and Shackleton: implications for regional geology, surface processes, and volatile sequestration. *Icarus* 255, 70–77. <https://doi.org/10.1016/j.icarus.2015.03.016>.
- Ward, W.R., 1975. Past orientation of the lunar spin axis. *Science* 189, 377–379.
- Watson, K., Murray, B.C., Brown, H., 1961. The behavior of volatiles on the lunar surface. *J. Geophys. Res.* 66, 3033–3045.
- Wieczorek, M.A., et al., 2013. The crust of the moon as seen by GRAIL. *Science* 339 (6120), 671–675. <https://doi.org/10.1126/science.1231530>.
- Wiggins, S.E., Johnson, B.C., Bowling, T.J., Melosh, H.J., Silber, E.A., 2019. Impact fragmentation and the development of the deep lunar megaregolith. *J. Geophys. Res. Planets* 124, 941–957. <https://doi.org/10.1029/2018JE005757>.
- Wilhelms, D.E., 1987. Geologic history of the Moon. In: *U. S. Geological Survey. Prof. Pap.* 1348, (302 pp).
- Wilkison, S.L., McCoy, T.J., McCamant, J.E., Robinson, M.S., Britt, D.T., 2003. Porosity and density of ordinary chondrites: clues to the formation of friable and porous ordinary chondrites. *Meteorit. Planet. Sci.* 38, 1423–1548. <https://doi.org/10.1111/j.1945-5100.2003.tb00256.x>.
- Wünnemann, K., Ivanov, B.A., 2003. Numerical modelling of the impact crater depth-diameter dependence in an acoustically fluidized target. *Planet. Space Sci.* 51, 831–845. <https://doi.org/10.1016/j.pss.2003.08.001>.
- Wünnemann, K., Morgan, J.V., Jödicke, H., 2005. Is Ries crater typical for its size? An analysis based upon old and new geophysical data and numerical modeling. *GSA Special Paper* 384. <https://doi.org/10.1130/0-8137-2384-1.67>.
- Wünnemann, K., Collins, G.S., Melosh, H.J., 2006. A strain-based porosity model for use in hydrocode simulations of impacts and implications for transient crater growth in porous targets. *Icarus* 180 (2), 514–527. <https://doi.org/10.1016/j.icarus.2005.10.013>.
- Yamamoto, S., Nakamura, R., Matsunaga, T., Ogawa, Y., Ishihara, Y., Morota, T., 2012. Massive layer of pure anorthosite on the moon. *Geophys. Res. Lett.* 39, L13201 <https://doi.org/10.1029/2012GL05209>.
- Zhu, M., Wünnemann, K., Potter, R.W.K., 2015. Numerical modeling of the ejecta distribution and formation of the Orientale basin on the moon. *J. Geophys. Res. Planets* 120 (12), 2118–2134. <https://doi.org/10.1002/2015je004827>.
- Zuber, M.T., et al., 2012. Constraints on the volatile distribution within Shackleton crater at the lunar south pole. *Nature* 486, 378–381. <https://doi.org/10.1038/nature11216>.
- Zuber, M.T., Smith, D.E., Lehman, D.H., et al., 2013. Gravity Recovery and Interior Laboratory (GRAIL): Mapping the Lunar Interior from Crust to Core. *Space Sci Rev* 178, 3–24. <https://doi.org/10.1007/s11214-012-9952-7>.